Electronic Supplementary Material (ESI) for Journal of Materials Chemistry A.

Supporting Information

Self-stacked multilayer FeOCl supported on a cellulose-derived carbon aerogel: A new and high-performance anode material for supercapacitors

Caichao Wan,[a] Yue Jiao,[b] Wenhui Bao,[b] He Gao,[b] Yiqiang Wu,*[a] Jian Li*[b]*

[a]College of Materials Science and Engineering, Central South University of Forestry and Technology, Changsha 410004, P. R. China

[b]Material Science and Engineering College, Northeast Forestry University, Harbin 150040, P. R. China

*Corresponding authors. E-mails: wancaichaojy@163.com (C. Wan); wuyq0506@126.com (Y. Wu); nefulijian@163.com (J. Li)

Outlines

1. Experimental Section

Reagents and materials: Chemicals including sodium sulfate (Na_2SO_4), magnesium sulfate ($MgSO_4$), sodium hydroxide (NaOH), polyethylene glycol-4000 (PEG-4000), tert-butyl alcohol, α-Fe_2O_3, anhydrous $FeCl_3$ and manganese dioxide (MnO_2) were obtained from Shanghai Aladdin Industrial Inc. (China). Bamboo fiber was supplied by Zhejiang Mingtong Textile Technology Co., Ltd. and further washed several times with distilled water and dried at 60 °C for 24 h. The dried bamboo fiber was directly used as cellulose feedstock without further purification. Polytetrafluoroethylene (PTFE) plates were purchased from Dahua Plastic Industry Co., Ltd. (Hangzhou, China). Superfine acetylene black, nickel (Ni) foam and PTFE binder were supplied by China New Metal Materials Technology Co., Ltd.

Preparation of FeOCl: The preparation of FeOCl was carried out via a chemical-vapor-transport technique.[1] α-Fe_2O_3 was mixed with anhydrous $FeCl_3$ based on a molar ratio of 1:1.3. The obtained powder was sealed in a glass container. The sealed container was transferred to a muffle furnace and then heated to 380°C for 40 h. After washing with anhydrous acetone for the removal of excess $FeCl_3$ and vacuum drying at 40°C overnight, dark purple powder was obtained finally.

Preparation of FeOCl@CDCA: The synthesis of cellulose aerogel (the precursor of cellulose-derived carbon aerogel, CDCA) primarily includes three procedures: (1) dissolving the bamboo fiber in the solution of NaOH and PEG-4000; (2) regenerating the cellulose solution in a 1 v% HCl solution; (3) freeze-drying the resultant cellulose hydrogel after the solution replacement with tertiary butanol. The cellulose aerogel was

pyrolyzed to acquire CDCA under nitrogen environment. Detailed process is available in our previous reports.[2-4] CDCA and FeOCl were mixed by ball-milling with a mass ratio of 1:4. The ball-milling was performed in a planetary ball-mill (Changsha Deco Equipment Co., Ltd, China) with a rotation speed of 250 r/min using a 50 ml zirconia vial with zirconia balls (10 mm in diameter) under an argon atmosphere. The ball to powder ratio is 40:1 and the milling time is 1 h.

Fabrication of anode, cathode and ASC device: The FeOCl@CDCA, acetylene black and PTFE were mixed in a mass ratio of 70:20:10 and then ground in alcohol. It is worth mentioning that the addition of superfine acetylene black with a high electrical conductivity of ~400 S m^{-1} is helpful to ensure high inter-particle electric conductivity (like tunnel current), notwithstanding that CDCA is also conductive. The resultant slurry was pasted and pressed onto a Ni foam substrate at 10 MPa and then dried at 80 °C overnight, acting as an anode. A cheap and commercially available MnO_2 powder was also mixed with acetylene black and PTFE and the mixture was pressed onto a Ni foam according to the above process. This MnO_2 electrode serves as a cathode. The exposed geometric area of these electrodes equals to 1×1 cm^2. For the assembly of an asymmetric supercapacitor (ASC), a piece of common and thin cellulose paper acts as a separator. These electrodes and separator were sandwiched between two PTFE plates and the whole device was clamped by a high-strength plastic clamp.

Characterizations: Morphology was observed by a scanning electron microscope (SEM, Hitachi S4800). Transmission electron microscope (TEM) were performed with a FEI, Tecnai G2 F20 TEM with a field-emission gun operating at 200 kV. X-ray

diffraction (XRD) analysis was implemented on a Bruker D8 Advance TXS XRD instrument with Cu Kα (target) radiation (λ = 1.5418 Å) at a scan rate (2θ) of 4° min^{-1} and a scan range from 5 to 90°. X-ray photoelectron spectroscopy (XPS) was carried out on a Thermo Escalab 250Xi system using a spectrometer with a dual Al Ka X-ray source. Deconvolution of overlapped peaks was performed by a mixed Gaussian–Lorentzian fitting program (Origin 9.0, Originlab Corporation). N_2 adsorption–desorption tests were performed at –196°C on an accelerated surface area and porosimetry system (3H-2000PS2 unit, Beishide Instrument S&T Co., Ltd). Raman spectrum was measured using a Raman spectrometer (Renishaw, inVia) with a 633 nm He-Ne laser. Electrical conductivity was tested using a H7756 four-point probe resistivity meter with a testing range of 10^{-5}~10^{5} S cm^{-1} (Beijing Heng Odd Instrument Co., Ltd) at room temperature.

Electrochemical characterizations: Electrochemical properties of FeOCl@CDCA electrode were investigated by a CS350 electrochemical workstation (Wuhan CorrTest Instruments Corp., Ltd., China) in a three-electrode system: FeOCl@CDCA serves as the working electrode, and an Ag/AgCl electrode and a Pt foil serve as reference and counter electrodes, respectively. The electrolyte is 1 M Na_2SO_4 aqueous solution. Cyclic voltammetry (CV) and galvanostatic charge–discharge (GCD) plots were tested over the potential window of –1 to 0 V. Electrochemical impedance spectroscopy (EIS) tests were carried out in the frequency range from 10^5 to 0.01 Hz with alternate current amplitude of 5 mV. The exposed geometric area of FeOCl@CDCA working electrode is equal to 1×1 cm^2 and the mass loading of electrochemically active substance (i.e., FeOCl and CDCA) per area is ~2.5 mg cm^{-2}. Also, the mass loading of active substance

per area is controlled to be ~2.5 mg cm^{-2} for CDCA, FeOCl and MnO_2 electrodes (these materials also underwent the ball-milling treatment before mixing with the PTFE and acetylene black). The working potential window of the FeOCl and CDCA electrodes is same with that of FeOCl@CDCA electrode, while the working potential window of the MnO_2 electrode is 0–0.8 V. For the MnO_2//FeOCl@CDCA ASC device, it was soaked in an aqueous electrolyte of 1 M Na_2SO_4 for all of the electrochemical tests in a two-electrode system. The geometric area of ASC equals to 1×1 cm^2.

Calculations: For CDCA, FeOCl, FeOCl@CDCA and MnO_2 electrodes and the assembled ASC, the gravimetric (C_m, F g^{-1}) and areal (C_s, F cm^{-2}) specific capacitances are calculated based on GCD curves at different current densities according to following equations:[5]

$$C_m = I\Delta t / m\Delta V \quad \text{or} \quad C_s = I\Delta t / s\Delta V \tag{1}$$

where I (A) is the discharge current, Δt (s) is the discharge time, m (g) is the mass of active materials, s is the specific area (cm^2), and ΔV (V) is the operation discharge voltage window. For the ASC, m (g) is the total mass of active materials in both anode and cathode electrodes (namely 5 mg).

The areal (E_s) or gravimetric (E_g) energy density and areal (P_s) or gravimetric (P_g) power density are evaluated on the basis of capacitance values shown as follows:[6]

$$E_s = \frac{1}{2} C_s (\Delta V)^2 / 3600 \quad \text{or} \quad E_m = \frac{1}{2} C_m (\Delta V)^2 / 3600 \tag{2}$$

$$P_s = \frac{E_s}{\Delta t} \times 3600 \quad \text{or} \quad P_m = \frac{E_m}{\Delta t} \times 3600 \tag{3}$$

2. Calculation of interlayer spacing of the FeOCl

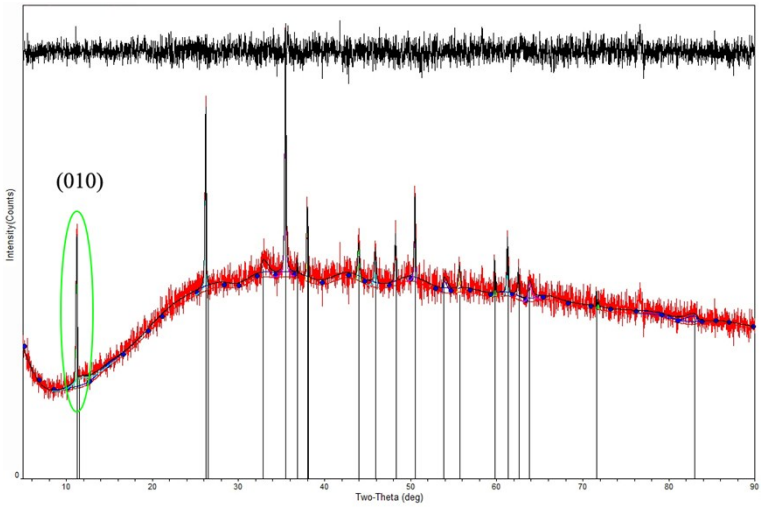

Figure S1. XRD pattern (thick red line) and Rietveld fit (thin black line) of FeOCl@CDCA. Rietveld fit, which was implemented by the MDI-JADE 6 program (Materials Data Inc., Livermore, CA, USA), was used to obtain the interlayer spacing of the FeOCl in FeOCl@CDCA.

FeOCl is a laminated compound and its "Van der Waals layer" suits for intercalation reactions by transferring charges between intercalated compounds and FeOCl matrix. Moreover, the space between layers can serve as a channel for migration and reactions of electrolyte ions when the interlayer spacing is larger than the hydrated ionic diameter. According to the XRD pattern (Figure 1i) and fitting results (Figure S1), the interplanar spacing of (010) plane (i.e., the interlayer spacing) can be calculated by the Bragg's equation:[7]

$$d = \frac{\lambda}{2\sin\theta} \tag{4}$$

where d is the interplanar spacing, λ is the wavenumber of X-ray and θ is the diffraction angle. Through calculation, the value of d_{010} is 0.783 nm.

3. Raman spectra of CDCA, FeOCl and FeOCl@CDCA

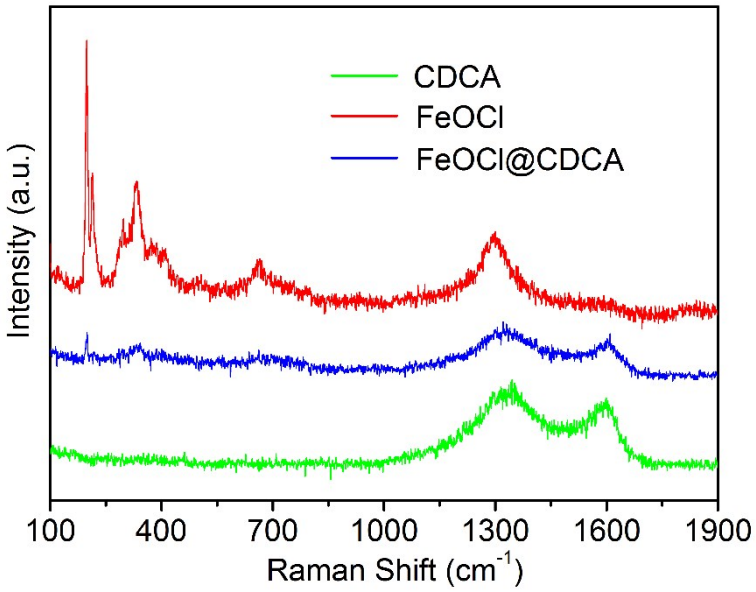

Figure S2. Raman spectra of CDCA, FeOCl and FeOCl@CDCA.

The Raman spectra of CDCA, FeOCl and FeOCl@CDCA are shown in Figure S2. Since the reports on Raman spectroscopy of FeOCl are rare, the assignment of the bands for FeOCl is referred to those for γ-FeOOH (lepidocrocite) because of their similarity on the structure. The strong peak at 199 cm^{-1} is possibly derived from the Fe–Cl bond.[8] The board peak at 334 cm^{-1} may be attributed to the Fe–OH bond.[9] For FeOCl@CDCA, these two characteristic peaks of FeOCl are still maintained and we also can find two new bands centered at 1340 cm^{-1} and 1600 cm^{-1}. The band at 1340 cm^{-1} (*D*-band) is associated with the disorder-induced scattering produced by imperfections or loss of hexagonal symmetry in the carbon structure.[10] This band is attributed to the A_{1g} mode and does not appear in perfect graphite crystals. Another band at 1600 cm^{-1} (*G*-band) is associated with the Raman active $2E_{2g}$ mode in two-dimensional network structure is always observed in all carbon and graphite materials.[11] These two characteristic

bands of carbon materials can also be identified in the Raman spectrum of CDCA. Thus, the result demonstrates the co-presence of CDCA and FeOCl in the composite.

The relative intensities (I_D/I_G) can be used to analyze the amount of carbon defects in CDCA and FeOCl@CDCA. A low I_D/I_G ratio reveals the presence of a larger amount of sp^2-coordinated carbon.[12] It can be seen that the I_D/I_G ratio increases from 1.234 for CDCA to 1.263 for FeOCl@CDCA. This increment is due to the introducing of FeOCl which slightly increases defects and disorders in CDCA.

4. Morphology of CDCA

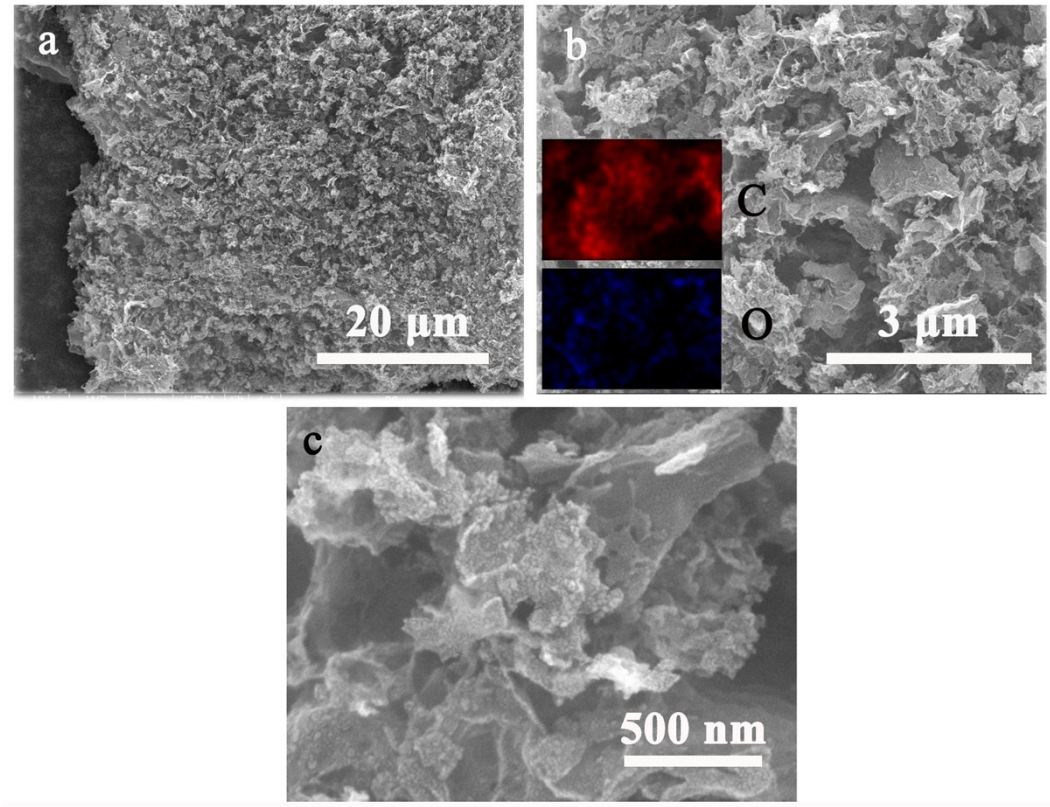

Figure S3. SEM images of CDCA at different magnifications, and the insets of *b* show the element mappings.

The micromorphology of CDCA was analyzed by SEM. As shown in Figure S3a and b, CDCA displays a 3D porous structure and the diameters of these pores range from nanoscale to microscale. This hierarchical and multiscale porous structure is helpful for the storage of electrolyte (shortening the diffusion distance of electrolyte ions) and migration of ions.

5. Surface area and pore size distribution of CDCA

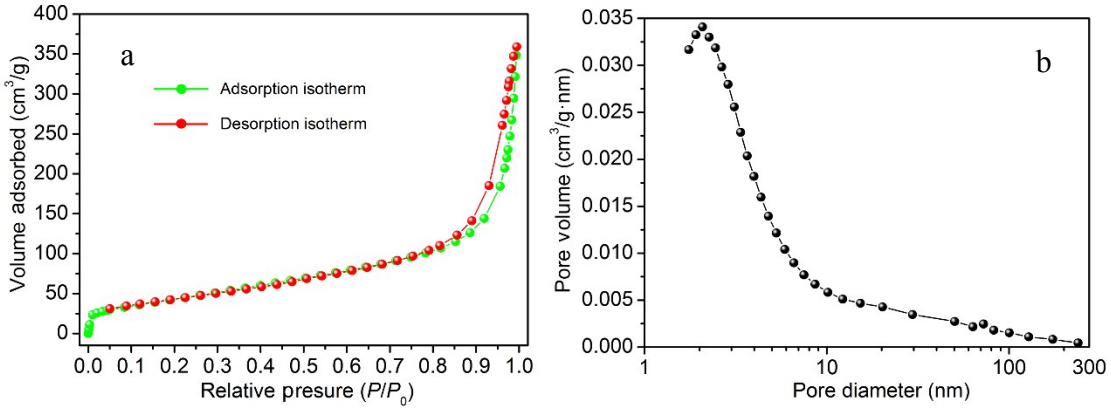

Figure S4. (a) N_2 adsorption–desorption isotherms and (b) pore size distribution of CDCA.

The specific surface area of CDCA is calculated over a relative pressure range of 0.05−0.30 by the multipoint Brunauer−Emmett−Teller (BET) method. The nitrogen adsorption volume at the relative pressure (P/P_0) of 0.994 is employed to determine the pore volume. The result indicates that the surface area and pore volume of CDCA are ~157 m^2 g^{-1} and ~0.53 cm^3 g^{-1}, similar to some previously reported data.[13-15] In addition, we can find that the surface area of CDCA is far larger than that of the FeOCl (~40 m^2 g^{-1}). Thus, the combination of CDCA with the FeOCl is expected to increase the reaction area and electrical conductivity of FeOCl@CDCA.

According to the N_2 adsorption–desorption isotherms of CDCA (Figure S4a), the adsorption uptakes in the P/P_0 range of 0 and 0.05 increase sharply, indicating the existence of micropores (<2 nm). Thereafter, the isotherms form an obvious hysteresis loop and still do not reach a plateau near the P/P_0 of 1.0, indicating the co-presence of mesopores (2–50 nm) and macropores (>50 nm). The pore size distribution is calculated from the data of the adsorption branch by the Barrett−Joyner−Halenda (BJH) method. The result presents that the pore sizes are in the range of 1.7–239 nm (Figure S4b),

agreeing well with the speculation from the isotherms. Such a pore size distribution is favorable for electrolyte penetration, allowing reaction species to quickly access the electrode.[16]

6. CV curves of the Ni foam

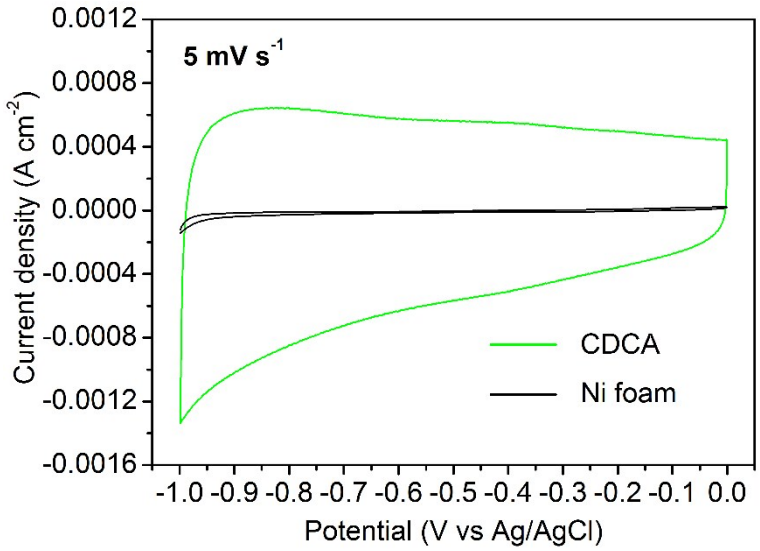

Figure S5. CV curves of CDCA and Ni foam at the scan rate of 5 mV s^{-1}.

The CV curves of CDCA and Ni foam are shown in Figure S5. The area enclosed within CV curves corresponds to the energy storage capability. The area enclosed within the CV curve of CDCA (the smallest area among those of CDCA, FeOCl and FeOCl@CDCA, Figure 2c) is much larger than that of the Ni foam, demonstrating that the contribution of the Ni foam to the capacitance is negligible.

7. CV curves of CDCA and FeOCl electrodes

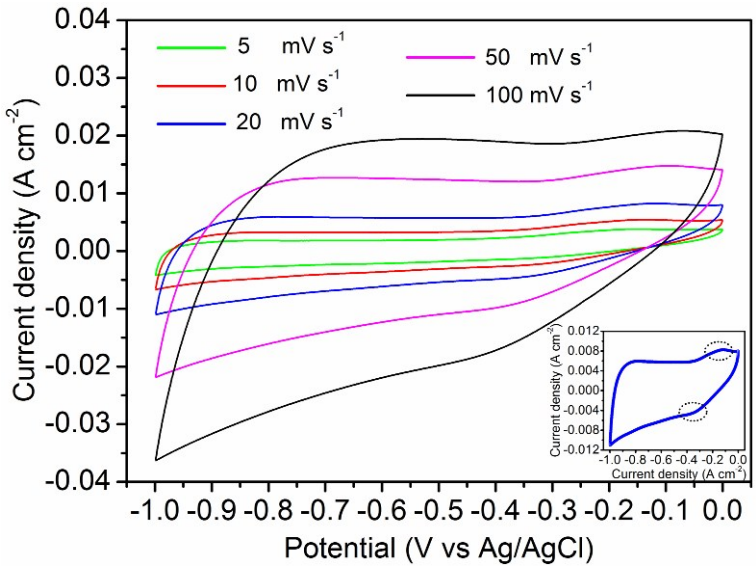

Figure S6. CV curves of the FeOCl electrode at scan rates of 5–100 mV s^{-1}, and the inset shows the enlarged image of CV curve at 20 mV s^{-1}.

The CV curves of the FeOCl electrode at scan rates of 5–100 mV s^{-1} are presented in Figure S6, where a pair of redox peaks are identified and reflect a pseudocapacitive charging mechanism. In addition, the potential of the cathodic peaks shifts towards the negative direction while that of the anodic peaks shifts towards the positive direction with the increasing scan rate. This phenomenon is associated with the internal resistance of the electrode and further suggests the pseudocapacitive features.[17]

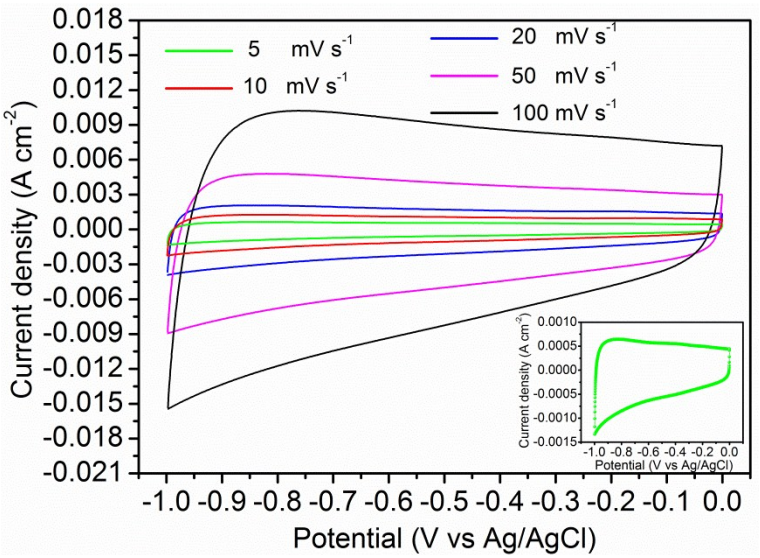

Figure S7. CV curves of CDCA electrode at scan rates of 5–100 mV s^{-1}, and the inset shows the enlarged image of CV curve at 5 mV s^{-1}.

The CV curves of CDCA electrode at scan rates of 5–100 mV s^{-1} are presented in Figure S7, where a quasi-rectangular shape is identified for these CV curves and reflects an electrochemical double-layer capacitance (EDLC) feature. At the same scan rate, it is clear that the area enclosed within the CV curve of CDCA is obviously smaller than that of the FeOCl, representing a stronger energy storage capability of the FeOCl. The phenomenon is common between ELDC materials and pseudocapacitance materials due to the difference in energy storage mechanisms.[18]

8. XPS spectrum of FeOCl@CDCA after electrochemical tests

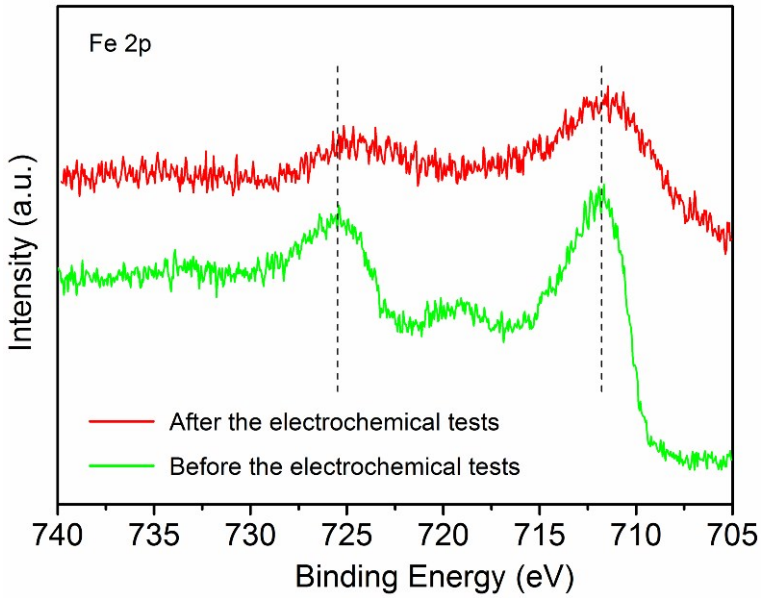

Figure S8. XPS spectrum of Fe 2p in FeOCl@CDCA before and after electrochemical tests.

To study changes of chemical state of Fe element before and after electrochemical tests, the XPS spectra of FeOCl@CDCA were tested and compared. As shown in Figure S8, the Fe $2p_{3/2}$ peak is narrower and stronger than the Fe $2p_{1/2}$ peak and the area of Fe $2p_{3/2}$ peak is greater than that of Fe $2p_{1/2}$ because in spin–orbit (j–j) coupling; Fe $2p_{3/2}$ has degeneracy of four states whilst Fe $2p_{1/2}$ has only two.[19] Before the tests, the peak positions of Fe $2p_{3/2}$ and Fe $2p_{1/2}$ are located at ~711.6 and 725.4 eV, suggesting that the Fe element appears as Fe(III) state.[20] In addition, it is known that the Fe $2p_{3/2}$ peak has associated satellite peaks and the satellite peak of Fe $2p_{3/2}$ for Fe(III) is generally located approximately 8 eV higher than the main Fe $2p_{3/2}$ peak.[21, 22] In Figure S8, the shake-up satellite of Fe $2p_{3/2}$ is situated at 719.3 eV, which is further representative of Fe (III). For Fe(II) state in FeO, peak positions of Fe $2p_{3/2}$ and Fe $2p_{1/2}$ move to lower binding energies, around 2 eV lower than those of Fe_2O_3.[19] After the tests, it is obvious

that the peaks of Fe $2p_{3/2}$ and Fe $2p_{1/2}$ shift to lower binding energies of 711.2 and 724.2 eV, respectively, indicative of the partial reduction of Fe(III) in FeOCl@CDCA.

9. CV and GCD plots of FeOCl@CDCA electrode tested in $MgSO_4$ electrolyte

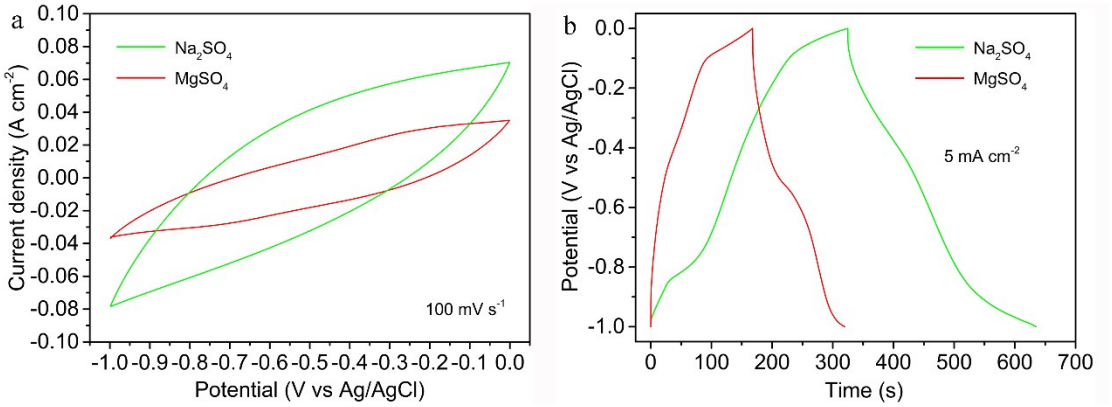

Figure S9. Comparison of (a) CV and (b) GCD plots of FeOCl@CDCA electrode tested in $MgSO_4$ and Na_2SO_4 electrolytes

To strengthen the validation of the proposed Na^+-intercalation mechanism, the CV and GCD curves of FeOCl@CDCA were also measured in 1 M $MgSO_4$ electrolyte. As the hydrated ionic diameter of Mg^{2+} (0.856 nm)[23] is larger than that of the interlayer distance of FeOCl (0.783 nm), a notably decreased capacitance measured in the $MgSO_4$ electrolyte will help to demonstrate the intercalation mechanism. The detailed analyses are avalible in the main body.

10. Calculation of apparent diffusion coefficients

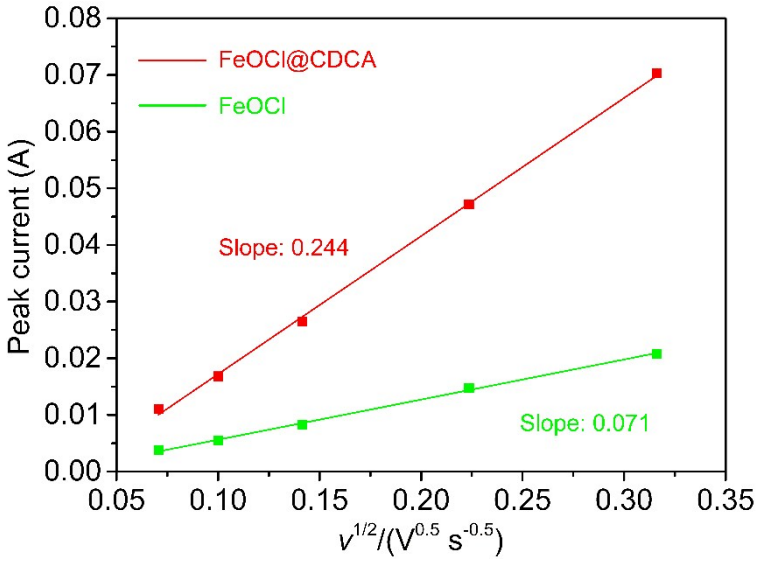

Figure S10. Apparent diffusion coefficients of FeOCl@CDCA and FeOCl electrodes calculated by the Randles–Sevick equation.[24]

According to the Randles–Sevick equation,[24] the apparent diffusion coefficients of the FeOCl and FeOCl@CDCA electrodes are calculated and comapred for further studying their ionic transport process. The coefficients can be determined by the slope of "peak current–(scan rate)$^{1/2}$" plots. A higher value represents a faster ionic diffusion rate. The detailed analyses are avalible in the main body.

11. GCD plots of CDCA and FeOCl electrodes

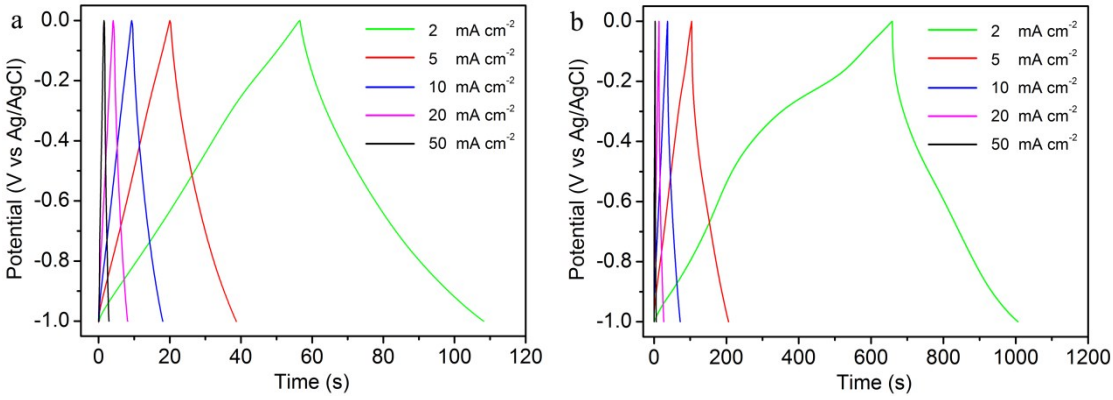

Figure S11. GCD plots of (a) CDCA and (b) FeOCl electrodes at current densities of 2–50 mA cm^{-2}.

The GCD plots of CDCA and FeOCl electrodes are exhibited in Figure S11. As seen in Figure S11a, the charge curves of CDCA electrode are almost symmetric to their discharge counterparts without remarkable curvature, which reveals main contributions from EDLC. Also, no obvious IR drop appears, suggesting that CDCA possesses rapid I–V response ability and low internal resistance. In addition, the distinct curvature is identified for the GCD plots of the FeOCl (Figure S11b), reflecting its pseudocapacitive charging mechanism. Based on the discharge curves, the areal specific capacitances of the FeOCl are calculated as 696, 510, 351, 264 and 150 mF cm^{-2} at current densities of 2, 5, 10, 20 and 50 mA cm^{-2}. Moreover, the areal specific capacitances of CDCA are 103, 94, 87, 82 and 70 mF cm^{-2} at 2, 5, 10, 20 and 50 mA cm^{-2}. We can find that CDCA shows a more superior rate performance with a higher capacitance retention of 68% than that of the FeOCl (only 22%). We integrate the FeOCl with CDCA (only 4:1 ratio) by the ball-milling method and the resultant composite presents a remarkably enhanced rate capability of 54%, demonstrating the significance of combination.

12. Cycle stability and coulombic efficiency of the FeOCl electrode

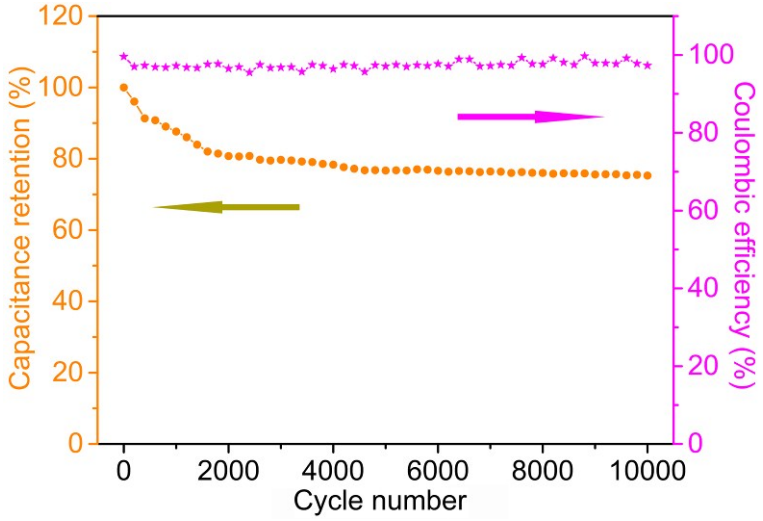

Figure S12. Cycle stability and coulombic efficiency of the FeOCl electrode at 50 mA cm^{-2}.

The cycle stability and coulombic efficiency of the FeOCl electrode at 50 mA cm^{-2} are shown in Figure S12. The FeOCl shows a capacitance retention of ~75% after 10000 cycles, obviously lower than that of FeOCl@CDCA (~91%, Figure 3c). This result indicates that the incorporation of CDCA improves the structural stability and cycle behavior of the FeOCl composition. In addition, the FeOCl maintains a high coulombic efficiency of 95%–100%, which is similar to that of FeOCl@CDCA (96%–100%).

13. Calculation of FeOCl theoretical specific capacitance

The theoretical pseudocapacitance of FeOCl is calculated based on the following equation:[25]

$$C = \frac{n \times F}{M \times V} \tag{5}$$

where n is the mean number of the electrons transferred in the redox reaction, F is the Faraday constant, M is the molar mass of the metal oxide and V is the operating voltage window. Therefore, we can acquire the theoretical capacitance of FeOCl as: $(1 \times 96485.3383/1.0/107.2971)$ F $g^{-1} \approx 899$ F g^{-1}.

14. Electrochemical properties of the MnO_2 electrode

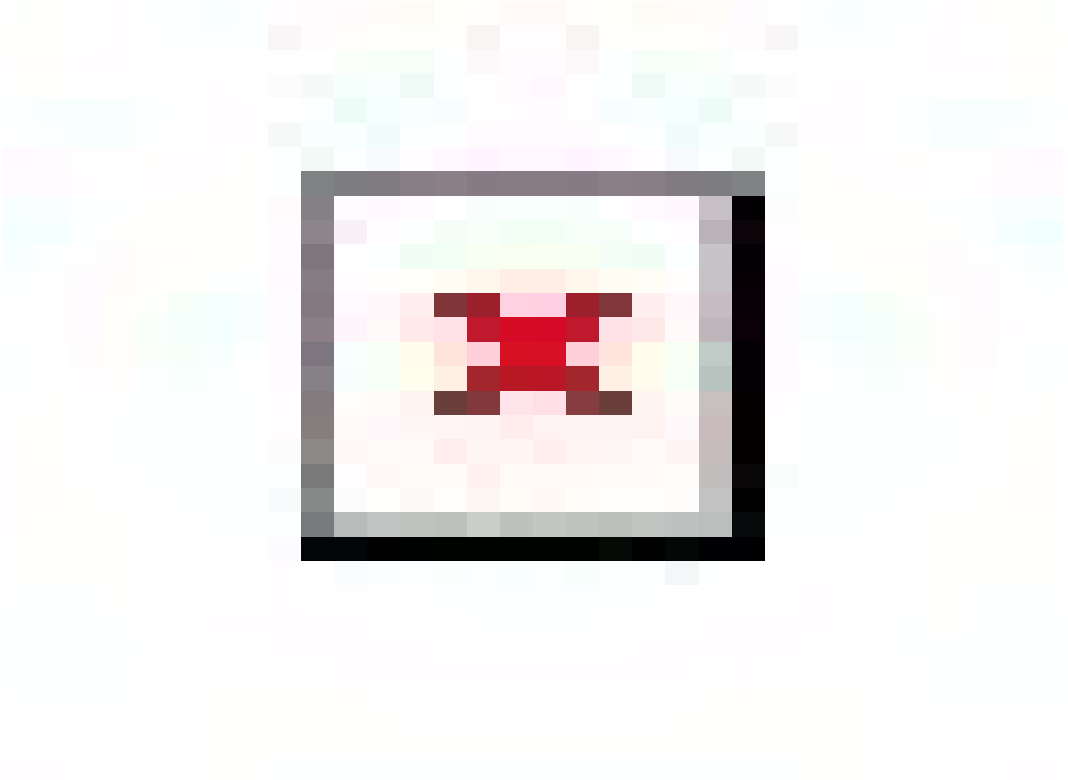

Figure S13. Electrochemical properties of the MnO_2 electrode: (a) CV curves at scan rates of 5–100 mV s^{-1}, and the inset shows the enlarged image of the CV curve at 5 mV s^{-1}; (b) GCD curves at current densities of 2–50 mA cm^{-2}; (c) rate performance; (d) Nyquist plot and the inset shows the enlarged image at the high-frequency region.

The low-cost MnO_2 electrode was chosen as a cathode to assemble an ASC with FeOCl@CDCA as an anode. The electrochemical performances of the MnO_2 electrode were studied by CV, GCD and EIS in a three-electrode system. Its CV responses at different scan rates are displayed in Figure S13a. The relatively symmetrical rectangular shape indicates that the electrode has an ideal electrochemical capacitance behavior. In addition, during the charging–discharging steps (Figure S13b), the charging curves of the electrode are almost symmetric to their corresponding discharge

counterparts with slight curvature, indicating contributions from both pseudocapacitive and double layer. Based on the equation 1, the areal specific capacitances of the MnO_2 electrode can be calculated as 318, 285, 261, 228 and 169 mF cm^{-2} (127, 114, 104, 91 and 68 F g^{-1}) at the current densities of 2, 5, 10, 20 and 50 mA cm^{-2} (Figure S13c). Although the values are slightly lower than those of some previously reported MnO_2-based electrodes,[26-29] the electrode has some important advantages including simple preparation process and low cost, which may be more appropriate for large-scale production. In addition, a high capacitance retention of 53% with the increase of the current density from 2 to 50 mA cm^{-2} reflects its good rate property. EIS was applied to quantify their conductive and diffusive behavior. As seen in Figure S13d, the electrode has a low solution resistance and charge transfer resistance and the nearly vertical line in the low-frequency region suggests its good capacitive behavior.

15. Tables

Table S1. Physical and electrochemical properties reported in recent literature for anode materials in various aqueous electrolytes.

Electrode	Capacitance/F g^{-1}	Cycling stability	Surface area/m^2 g^{-1}	Electrolyte	Potential range/V	Mass loading/ mg cm^{-2}	Ref.[c]
γ-Fe_2O_3/graphene	76 (25 mV s^{-1})	97% (1000 cycles)	–	1 M Na_2SO_3	–0.8~0	1.25	35
Mesoporous MoO_2	146 (5 mV s^{-1})	90% (1000 cycles)	69	1 M LiOH	−0.5~−1.2	4	36
Polypyrrole@V_2O_5	308 (0.1 A g^{-1})	–	–	0.5 M K_2SO_4	–0.9~0.1	6	12
Ti–Fe_2O_3@PEDOT[a]	311.6 (1 mA cm^{-2})	~100% (30000 cycles)	–	5 M LiCl	–0.8~0	3.7	37
Highly functionalized activated carbons	525 (0.25 A g^{-1})	90.6% (10000 cycles)	1217.1	1 M KOH	–1~0	1	38
Iron nanosheets/graphene	717 (2 mV s^{-1})	80% (1000 cycles)	218	6 M KOH	–1.2~0	–	39
FeOOH nanoparticles	1066 (1 A g^{-1})	91% (10000 cycles)	–	2 M KOH	–1.2~0	1.6	40
Nano-sized columned *β*-FeOOH	116 (0.5 A g^{-1})	–	–	1 M Li_2SO_4	−0.85~−0.1	10	41
FeOOH nanorod/carbon tube network	396 (0.5 A g^{-1})	83% (5000 cycles)	274	6 M KOH	−1.08~0	2	42
CDCA	41.2 (0.8 A g^{-1})	–	157	1 M Na_2SO_4	–1~0	2.5	This study
FeOCl	278 (0.8 A g^{-1})	75% (10000 cycles)	40	1 M Na_2SO_4	–1~0	2.5	This study
FeOCl@CDCA	647 (0.8 A g^{-1})	91% (10000 cycles)	56	1 M Na_2SO_4	–1~0	2.5	This study

[a]PEDOT: poly(3,4-ethylenedioxythiophene); [b]RGO: reduced graphene oxide; [c]Please find these references in the manuscript.

Table S2. Comparison of the areal specific capacitance, areal energy density and cycling stability of the MnO_2//FeOCl@CDCA ASC with some recently reported ASCs storing energy by Faradaic reactions.

Devices	Maximum areal specific capacitance (mF cm^{-2})	Maximum areal energy density (μW h cm^{-2})	Cycling stability	Potential range (V)	Electrolyte	Refs[e)]
CuSe@$Co(OH)_2$//AC[a)]	13.2 (0.3 mA cm^{-2})	5.1 (~165 μW cm^{-2})	80.4% (10000 cycles)	0–1.5	PVA/KOH	49
RGO/MnO_2//RGO[b)]	113 (0.01 A g^{-1})	35.1 (37.5 μW cm^{-2})	84% (3600 cycles)	0–1.5	1 M Na_2SO_4	50
RGO–Co_3O_4//RGO	136.6 (2 mA cm^{-2})	35.92 (1.38 mW cm^{-2})	95.5% (6000 cycles)	0–1.4	PVA/KOH	51
NC LDH NSs@Ag@CC//AC[c)]	230.2 (1 mA cm^{-2})	78.8 (785 μW cm^{-2})	88.1% (2000 cycles)	0–1.6	1 M KOH	52
$CoMoO_4$@Ni foam//AC	~417 (5 mA cm^{-2})	125 (1.5 mW cm^{-2})	–	0–1.5	2 M KOH	53
MnO/Au NP[d)]//Fe_3O_4/Au NP	344.1 (1 mA cm^{-2})	267.3 (~2 mW cm^{-2})	89.8% (5000 cycles)	0–2 V	1 M Na_2SO_4	54
MnO_2//FeOCl@CDCA	641 (2 mA cm^{-2})	289 (1.8 mW cm^{-2})	88.7% (10000 cycles)	0–1.8	1 M Na_2SO_4	This work

[a)]AC: activated carbon; [b)]RGO: reduced graphene oxide; [c)]NC LDH NSs@Ag@CC//AC: Nickel-cobalt layered double hydroxide nanosheets@Ag@carbon cloth//activated carbon; [d)]NC: nanoparticles; [e)]Please find these references in the manuscript.

References

[1] Herber, R. H., & Cassell, R. A. (1981). Synthesis, hyperfine interactions, and lattice dynamics of a crown ether intercalation compound of FeOCl. The Journal of Chemical Physics, 75(9), 4669-4678.

[2] Wan, C., & Li, J. (2015). Facile synthesis of well-dispersed superparamagnetic γ-Fe_2O_3 nanoparticles encapsulated in three-dimensional architectures of cellulose aerogels and their applications for Cr (VI) removal from contaminated water. ACS Sustainable Chemistry & Engineering, 3(9), 2142-2152.

[3] Wan, C., Lu, Y., Jiao, Y., Cao, J., Sun, Q., & Li, J. (2015). Preparation of mechanically strong and lightweight cellulose aerogels from cellulose-NaOH/PEG solution. Journal of Sol-Gel Science and Technology, 74(1), 256-259.

[4] Wan, C., & Li, J. (2016). Graphene oxide/cellulose aerogels nanocomposite: Preparation, pyrolysis, and application for electromagnetic interference shielding. Carbohydrate Polymers, 150, 172-179.

[5] Wang, J. G., Yang, Y., Huang, Z. H., & Kang, F. (2013). Effect of temperature on the pseudo-capacitive behavior of freestanding MnO_2@carbon nanofibers composites electrodes in mild electrolyte. Journal of Power Sources, 224, 86-92.

[6] Lu, Q., Lattanzi, M. W., Chen, Y., Kou, X., Li, W., Fan, X., Unruh, K. M., Chen, J. G., & Xiao, J. Q. (2011). Supercapacitor electrodes with high-energy and power densities prepared from monolithic NiO/Ni nanocomposites. Angewandte Chemie International Edition, 50(30), 6847-6850.

[7] Bond, W. L. (1960). Precision lattice constant determination. Acta Crystallographica, 13(10), 814-818.

[8] Yang, X. J., Tian, P. F., Zhang, X. M., Yu, X., Wu, T., Xu, J., & Han, Y. F. (2015). The generation of hydroxyl radicals by hydrogen peroxide decomposition on FeOCl/SBA-15 catalysts for phenol degradation. AIChE Journal, 61(1), 166-176.

[9] Avery, J. S., Burbridge, C. D., & Goodgame, D. M. L. (1968). Raman spectra of tetrahalo-anions of FeIII, MnII, FeII, CuII and ZnII. Spectrochimica Acta Part A: Molecular Spectroscopy, 24(11), 1721-1726.

[10] Ferrari, A. C., & Robertson, J. (2000). Interpretation of Raman spectra of disordered and amorphous carbon. Physical review B, 61(20), 14095.

[11] Maldonado-Hódar, F. J., Moreno-Castilla, C., Rivera-Utrilla, J., Hanzawa, Y., & Yamada, Y. (2000). Catalytic graphitization of carbon aerogels by transition metals. Langmuir, 16(9), 4367-4373.

[12] Ji, L., Toprakci, O., Alcoutlabi, M., Yao, Y., Li, Y., Zhang, S., Guo, B., & Zhang, X. (2012). α-Fe_2O_3 nanoparticle-loaded carbon nanofibers as stable and high-capacity anodes for rechargeable lithium-ion batteries. ACS Applied Materials & Interfaces, 4(5), 2672-2679.

[13] Grzyb, B., Hildenbrand, C., Berthon-Fabry, S., Bégin, D., Job, N., Rigacci, A., & Achard, P. (2010). Functionalisation and chemical characterisation of cellulose-derived carbon aerogels. Carbon, 48(8), 2297-2307.

[14] Meng, Y., Young, T. M., Liu, P., Contescu, C. I., Huang, B., & Wang, S. (2015). Ultralight carbon aerogel from nanocellulose as a highly selective oil absorption material. Cellulose, 22(1), 435-447.

[15] Wan, C., Lu, Y., Jiao, Y., Jin, C., Sun, Q., & Li, J. (2015). Fabrication of hydrophobic, electrically conductive and flame-resistant carbon aerogels by pyrolysis of regenerated cellulose

aerogels. Carbohydrate Polymers, 118, 115-118.

[16] Saliger, R., Fischer, U., Herta, C., & Fricke, J. (1998). High surface area carbon aerogels for supercapacitors. Journal of Non-Crystalline Solids, 225, 81-85.

[17] Kumar, R., Rai, P., & Sharma, A. (2016). 3D urchin-shaped $Ni_3(VO_4)_2$ hollow nanospheres for high-performance asymmetric supercapacitor applications. Journal of Materials Chemistry A, 4(25), 9822-9831.

[18] Salanne, M., Rotenberg, B., Naoi, K., Kaneko, K., Taberna, P. L., Grey, C. P., Dunn, B., & Simon, P. (2016). Efficient storage mechanisms for building better supercapacitors. Nature Energy, 1(6), 16070.

[19] Yamashita, T., & Hayes, P. (2008). Analysis of XPS spectra of Fe^{2+} and Fe^{3+} ions in oxide materials. Applied Surface Science, 254(8), 2441-2449.

[20] Li, L., Chu, Y., Liu, Y., & Dong, L. (2007). Template-free synthesis and photocatalytic properties of novel Fe_2O_3 hollow spheres. The Journal of Physical Chemistry C, 111(5), 2123-2127.

[21] Hawn, D. D., & DeKoven, B. M. (1987). Deconvolution as a correction for photoelectron inelastic energy losses in the core level XPS spectra of iron oxides. Surface and Interface Analysis, 10(2-3), 63-74.

[22] Muhler, M., Schlögl, R., & Ertl, G. (1992). The nature of the iron oxide-based catalyst for dehydrogenation of ethylbenzene to styrene 2. Surface chemistry of the active phase. Journal of Catalysis, 138(2), 413-444.

[23] Nightingale Jr, E. R. (1959). Phenomenological theory of ion solvation. Effective radii of hydrated ions. The Journal of Physical Chemistry, 63(9), 1381-1387.

[24] Wang, X., Niu, C., Meng, J., Hu, P., Xu, X., Wei, X., Zhou, L., Zhao, K., Luo, W., Yan, M.,

& Mai, L. (2015). Novel $K_3V_2(PO_4)_3$/C bundled nanowires as superior sodium‐ion battery electrode with ultrahigh cycling stability. Advanced Energy Materials, 5(17), 1500716.

[25] Yu, X., Lu, B., & Xu, Z. (2014). Super long-life supercapacitors based on the construction of nanohoneycomb-like strongly coupled $CoMoO_4$–3D graphene hybrid electrodes. Advanced Materials, 26(7), 1044-1051.

[26] Lei, Z., Shi, F., & Lu, L. (2012). Incorporation of MnO_2-coated carbon nanotubes between graphene sheets as supercapacitor electrode. ACS Applied Materials & Interfaces, 4(2), 1058-1064.

[27] Peng, Y., Chen, Z., Wen, J., Xiao, Q., Weng, D., He, S., Geng, H., & Lu, Y. (2011). Hierarchical manganese oxide/carbon nanocomposites for supercapacitor electrodes. Nano Research, 4(2), 216-225.

[28] Chen, S., Zhu, J., Wu, X., Han, Q., & Wang, X. (2010). Graphene oxide−MnO_2 nanocomposites for supercapacitors. ACS Nano, 4(5), 2822-2830.

[29] Fan, Z., Yan, J., Wei, T., Zhi, L., Ning, G., Li, T., & Wei, F. (2011). Asymmetric supercapacitors based on graphene/MnO_2 and activated carbon nanofiber electrodes with high power and energy density. Advanced Functional Materials, 21(12), 2366-2375.